The Astrophysical Journal, 995:51 (9pp), 2025 December 10 https://doi.org/10.3847/1538-4357/ae1cc4

Continued Radio Observations of the Persistent Radio Source Associated with FRB 20190520B Provide Insights into Its Origin

Arvind Balasubramanian[1,2], Mohit Bhardwaj[3], and Shriharsh P. Tendulkar[2,4,5]

[1] Indian Institute of Astrophysics, Koramangala II Block, Bangalore 560034, India; arvind.balasubramanian@iiap.res.in
[2] Department of Astronomy and Astrophysics, Tata Institute of Fundamental Research, Mumbai 400005, India
[3] McWilliams Center for Cosmology, Department of Physics, Carnegie Mellon University, Pittsburgh, PA 15213, USA
[4] National Centre for Radio Astrophysics, Post Bag 3, Ganeshkhind, Pune 411007, India
[5] CIFAR Azrieli Global Scholars Program, MaRS Centre, West Tower, 661 University Avenue, Suite 505, Toronto, ON M5G 1M1, Canada

Received 2025 July 3; revised 2025 November 5; accepted 2025 November 5; published 2025 December 4

Abstract

Follow-up studies of persistent emission from fast radio burst (FRB) sources are critical for understanding their elusive emission mechanisms and the nature of their progenitors. This work presents new observations of the persistent radio source (PRS) associated with FRB 20190520B. We observe a gradual decay in the PRS brightness, which is punctuated by periods of brightening and dimming at both 1.5 and 3 GHz. Furthermore, our low-frequency ($<$1 GHz) observations—the first for this source—reveal evidence of a spectral break, which can be attributed to absorption processes. Interpreted within the framework of the magnetar wind nebula model, our data constrain the age of the magnetar progenitor to 52^{+16}_{-10} yr, broadly consistent with previous work. Assuming the observed 1.5 GHz variability is driven by scintillation, we discuss the constraints on the size of the persistent source. The observations presented here challenge the predictions of the previously published best-fit hypernebula model for this source.

Unified Astronomy Thesaurus concepts: Radio bursts (1339); Radio transient sources (2008); Transient sources (1851); Radio sources (1358)

1. Introduction

Fast radio bursts (FRBs) are highly energetic ∼millisecond-duration radio transients (D. R. Lorimer et al. 2007). The observations of FRBs using various radio facilities have revealed that some FRBs repeat, while others appear to be nonrepeating (E. Petroff et al. 2022). Among the FRBs that repeat, only two have shown evidence of a periodicity in their activity windows (E. Petroff et al. 2022, and references therein). FRBs experience propagation effects due to interaction and scattering before reaching our detectors. Some propagation effects include: dispersion measure (DM)—the delay in arrival of low-frequency radiation compared to the high-frequency radiation due to interaction with ionized medium; rotation measure (RM)—Faraday rotation of the polarization angle due to magnetic field along the line of sight. The measured DM of the FRB can be expressed as a sum of the DM contribution from the Milky Way, the interstellar medium, the intergalactic medium, and the local DM from the host galaxy of the FRB.

The origin of FRBs is still an open question, with many proposed models (E. Platts et al. 2019). The discovery of an FRB-like burst from galactic magnetar SGR 1935+2154 has bolstered interest in magnetar-based models as the leading candidates for explaining FRBs (C. D. Bochenek et al. 2020; CHIME/FRB Collaboration et al. 2020). To date, a total of ≈1000 FRB sources have been identified, of which $<10\%$ are repeaters (CHIME/FRB Collaboration et al. 2021, 2024; J. Xu et al. 2023, 2025). Less than 100 FRBs have been localized to their host galaxies, providing rich insights into FRB environments (see, e.g., S. Chatterjee et al. 2017; S. P. Tendulkar et al. 2021; B. Marcote et al. 2020; C. H. Niu et al. 2022). Among the population of repeating FRBs, a handful of sources are of particular interest given that a compact persistent radio source (PRS) has been observed associated with them—FRB 20121102 (S. Chatterjee et al. 2017), FRB 20190520B (C. H. Niu et al. 2022), FRB 20201124A (G. Bruni et al. 2024; Y. Bhusare et al. 2025), FRB 20190417A (A. M. Moroianu et al. 2025), and FRB 20181030A (A. L. Ibik et al. 2024).

FRB 20190520B was discovered by the Five-hundred-meter Aperture Spherical radio Telescope on 2019 May 20, as part of the CRAFT Survey (D. Li et al. 2018). It has been localized to a star-forming dwarf galaxy at a redshift of $z = 0.241$ (C. H. Niu et al. 2022; X.-L. Chen et al. 2025). The average DM of bursts from this source is $1207\,\mathrm{cm}^{-3}\,\mathrm{pc}$. Initially, the DM contribution from the host was thought to be exceptionally large, $\sim 900\,\mathrm{cm}^{-3}\,\mathrm{pc}$. However, K.-G. Lee et al. (2023) investigated the effect of foreground galaxies and estimated a substantially lower host DM (also see M. Bhardwaj et al. 2025). Observations of bursts from this FRB using the Green Bank Telescope and Parkes telescope by R. Anna-Thomas et al. (2023) have shown that the RM changes sign twice, pointing to a change in the magnetic field component parallel to the propagation, possibly due to a turbulent magnetized screen surrounding the FRB source. S. Bhandari et al. (2023) used very-long-baseline interferometry (VLBI) observations to constrain the size of the PRS < 9 pc and colocated it to within 80 pc of the FRB. This PRS exhibits a flat spectrum (slope of -0.4 at 2020 and -0.33 at 2021 epochs) above 1 GHz, accompanied by a ∼20% decline in broadband flux between the 2020 and 2021 epochs (X. Zhang et al. 2023). The PRS has not been detected at frequencies $<$1 GHz in the past.

Some leading models proposed to explain persistent radio emission from FRB sources are the magnetar wind nebula (MWN) model (B. Margalit & B. D. Metzger 2018) and the hypernebula model (N. Sridhar & B. D. Metzger 2022). The MWN model attributes persistent radio emission to synchrotron emission from magnetized electron–ion interactions with the nebula, powered by the flaring activity of a young magnetar. The hypernebula model explains the persistent emission as the interaction of winds emitted by an accreting black hole with the surrounding medium. Details of the interpretations of these models are discussed in Section 3.

In this paper, we present the first-ever low-frequency observations of the persistent radio source associated with FRB 20190520B. We interpret the temporal and spectral evolution of the persistent emission by combining our new observations and previous observations of the source. Section 2 describes the observations and data reduction performed, followed by Section 3 covering the analysis of the observations. Finally, we conclude with a discussion of our analysis in Section 4.

2. Observations

2.1. Upgraded Giant Metrewave Radio Telescope Observations and Archival Data

We observed the PRS associated with FRB 20190520B using the wideband receiver backend of the upgraded Giant Metrewave Radio Telescope (uGMRT) in three frequency bands: band 3 (central frequency, $\nu_c = 400$ MHz; bandwidth (BW) = 200 MHz), band 4 ($\nu_c = 750$ MHz; BW = 400 MHz), and band 5 ($\nu_c = 1260$ MHz; BW = 400 MHz) between 2023 June 16 and 2023 June 20 (Proposal 44_039, PI: Balasubramanian). The band 3 observations under this project were split over two days. We also obtained three epochs of observations each in band 4 and band 5 between 2024 September 5 and 2024 September 21 (Proposal 46_126, PI: Balasubramanian). In addition to our observations, we included archival uGMRT data from proposal 43_054 (PI: Y. Feng) in our analysis. Raw data were downloaded in the `FITS` format and converted to the `CASA` (CASA Team et al. 2022) measurement set format. The data were then calibrated and imaged using the automated continuum imaging pipeline `CASA-CAPTURE` (R. Kale & C. H. Ishwara-Chandra 2021). All observations used 3C286 as the flux calibrator. J1543-0757 was used as the phase calibrator for observations under 43_054 and 46_126, while J1558-1409 was used as the phase calibrator for observations under 44_039. For the band 3 data, the two measurement sets (under 44_039) were passed onto the automated pipeline separately and then imaged after combining the calibrated measurement sets. Each pipeline run included eight rounds of self-calibration. The band 5 flux density of the persistent source was calculated using the `CASA` task `imfit` within a small circular region (of radius ∼2× the size of the synthesized beam at band 5) centered at the PRS coordinates. An additional 5% flux density error was added in quadrature to the error obtained from `imfit` to account for flux calibration errors (see Table 1). No detections were made in band 3 or in any epoch of band 4 observations. The upper limit values listed in Table 1 are the 3× rms value within a large circular region (of radius ∼20× the size of the synthesized beam at the respective band) centered at the position of the PRS. None of the upper limits are used in the analyses in the section that follows. The observation on 2022 November 11 (under GMRT 43_053) shows a possible phase calibration issue, which was identified by imaging the flux calibrator using the same calibration solution (see Figure A1 in the Appendix for a comparison of the nondetection versus detection of the PRS and the flux calibrator). Additionally, the two observations on 2024 September 15 and 2024 September 21 (under 46_126) were affected by severe radio frequency interference, not allowing for sufficiently clean images.

2.2. Very Large Array Observations and Archival Data

We conducted a single *L*-band (∼1.5 GHz) observation of the PRS using the Jansky Very Large Array (VLA) on 2024 August 8. In addition, VLA *S*-band (∼3 GHz) data of the PRS20190520B field were obtained from the archival data listed under proposal 23A-010 (PI: Y. Feng, taken between 2023 June 7 and 2023 June 24). We obtained the calibrated measurement set when available or started with the raw data. Raw data were calibrated using the automated VLA calibration pipeline.[6] All observations used 3C286 as the flux calibrator. J1543-0757 was used as the phase calibrator for observations under 23A-010, while J1558-1409 was used as the phase calibrator for observations under 24A-409. Following calibration, the data were imaged using the automated imaging pipeline[7] and refined through self-calibration. The best self-calibrated image was selected, and the `CASA` task `imfit` was used in a small region around the PRS to estimate the source flux density. An additional 5% flux uncertainty was added in quadrature to account for flux calibration errors. It may be noted that the data under 23A-010 has already been analyzed using custom software based on the Astronomical Image Processing System[8] by A. Y. Yang et al. (2024). Here, we repeated the analysis of this data using the CASA VLA calibration pipeline to maintain consistency with the other measurements in this work. There are slight differences in the obtained measurements compared to the ones discussed in A. Y. Yang et al. (2024) due to the different calibration and imaging tools used here.

A summary of all measurements is listed in Table 1. Figure 1 shows the decay of the overall flux density of the PRS over time. Figure 2 shows the temporal variation of the PRS flux density at different frequency bands, and Figure 3 displays the variation of the spectrum over the epochs. We observe flaring and dimming episodes of the source in the ≈1.5 GHz data, especially in the late 2020 epoch. The possible reason for this observation is discussed in Section 3.3. For some observations, the image was heavily affected by radio frequency interference, resulting in an image that was insufficiently clean to use for our analysis (see Table 1 table note).

3. Physical Interpretations

Equipped with the newly observed multifrequency dataset of the PRS associated with FRB 20190520B, we present constraints on the physical properties of the possible progenitor of the persistent emission.

3.1. Monotonic Trend in the Observations

To investigate the presence of a monotonic trend in the light curve, we took all the observations listed in Table 1 and scaled the flux densities to 1.5 GHz, assuming a spectral index of −0.4 (as observed in X. Zhang et al. 2023, for the 2020 epoch). These scaled data were then subjected to the Mann–

---

[6] https://science.nrao.edu/facilities/vla/data-processing/pipeline/CIPL_654

[7] https://science.nrao.edu/facilities/vla/data-processing/pipeline/vipl_661_v2

[8] https://www.aips.nrao.edu/index.shtml

Table 1
Summary of Radio Continuum Observations of the Persistent Radio Source Associated with FRB 20190520B

Date	Time (MJD)	Frequency (GHz)	Flux Density (uJy)	Flux Density Error (uJy)	References
2020 Jul 21	59051.067	1.5	258	29	X. Zhang et al. (2023)
2020 Jul 23	59053.08	1.5	273	37	…
2020 Aug 18	59079.019	5.5	145	17	…
2020 Aug 18	59079.986	5.5	164	19	…
2020 Aug 29	59090.956	5.5	158	17	…
2020 Aug 30	59091.953	3.0	195	24	…
2020 Sep 12	59104.881	3.0	160	21	…
2020 Sep 12	59104.923	5.5	151	17	…
2020 Sep 13	59105.991	3.0	186	24	…
2020 Sep 15	59107.93	5.5	153	17	…
2020 Sep 19	59111.13	3.0	176	25	…
2020 Nov 8	59161.691	5.5	139	20	…
2020 Nov 14	59167.652	3.0	233	29	…
2020 Nov 16	59169.655	3.0	211	25	…
2021 Oct 1	59488.879	10.0	115	24	X. Zhang et al. (2023)
2021 Oct 1	59488.883	5.5	114	28	…
2021 Oct 1	59488.887	3.0	112	34	…
2021 Oct 1	59488.895	1.5	240	70	…
2021 Nov 7	59525.861	10.0	81	18	…
2021 Nov 7	59525.865	5.5	139	33	…
2021 Nov 7	59525.869	3.0	111	33	…
2021 Nov 7	59525.877	1.5	212	61	…
2022 Feb 26	59636.208	1.7	197	34	S. Bhandari et al. (2023)
2022 Feb 27	59637.208	1.7	210	34	…
[a] 2022 Nov 11	59894.205	1.3	…	…	GMRT 43_054 (This work)
2022 Nov 29	59912.125	1.3	268	44	…
2022 Dec 27	59940.131	1.3	156	26	…
2023 Jan 24	59968.036	1.3	281	41	…
2023 Feb 21	59996.167	1.3	119	36	…
2023 Mar 21	60024.962	1.3	280	25	…
2023 Jun 7	60102.323	3.0	157	9	VLA 23A-010 (This work)
2023 Jun 15	60110.234	3.0	173	11	…
2023 Jun 16	60111.84	0.7	$<$165	…	GMRT 44_039 (This work)
2023 Jun 17	60112.192	3.0	171	12	VLA 23A-010 (This work)
2023 Jun 18	60113.178	3.0	166	10	…
2023 Jun 18	60113.219	3.0	165	11	…
2023 Jun 19	60114.196	0.3	$<$195	…	GMRT 44_039 (This work)
2023 Jun 20	60115.172	3.0	152	10	VLA 23A-010 (This work)
2023 Jun 20	60115.214	3.0	151	11	…
2023 Jun 20	60115.255	3.0	143	10	…
2023 Jun 20	60115.297	3.0	152	10	…
2023 Jun 20	60115.584	1.3	179	18	GMRT 44_039 (This work)
2023 Jun 23	60118.262	3.0	147	13	VLA 23A-010 (This work)
2023 Jun 24	60119.168	3.0	155	15	…
2023 Jun 24	60119.209	3.0	144	13	…
2024 Aug 8	60530.985	1.5	221	13	VLA 24A-409 (This work)
2024 Sep 3	60556.588	1.3	230	24	GMRT 46_126 (This work)
2024 Sep 5	60558.585	0.7	$<$155	…	…
2024 Sep 12	60565.589	1.3	184	16	…
[b] 2024 Sep 15	60568.594	0.7	…	…	…
2024 Sep 21	60574.329	1.3	190	20	…
[b] 2024 Sep 21	60574.0	0.7	…	…	…

Notes. For nondetections, 3σ is the rms flux density measured in a large region of the residual image. Observation dates (in two formats), frequency bands, flux densities and their associated errors, and proposal identifiers/paper references are listed.

[a] Probable issue with phase calibration. See nondetection in Figure A1.

[b] Data affected by severe radio frequency interference. A sufficiently clean image was not obtained.

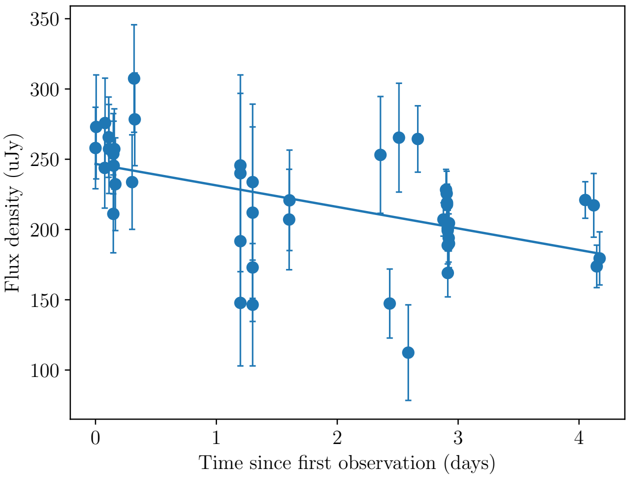

Figure 1. Light curve with all the flux density measurements from Table 1 scaled to 1.5 GHz assuming a spectral index of −0.4. The fit is a linear regression showing a decreasing trend in the overall flux density over time.

Kendall test using the `pymannkendall` package (M. Hussain & I. Mahmud 2019). The test yielded a p-value of 1.9×10^{-5} and a Kendall Tau value of −0.4, suggesting a significant decreasing trend. Figure 1 shows the light curve with the scaled flux density values along with the linear regression fit (slope = −15.3) performed with `scipy` package (P. Virtanen et al. 2020), showing the decreasing trend. Changing the assumed spectral index to −0.33 (as observed in X. Zhang et al. 2023, for the 2021 epoch) results in a similar Mann–Kendall p-value (2.8×10^{-4}), Kendall Tau value (−0.4), and linear regression fit (slope = −11.8) as above. This establishes a decreasing trend in the total flux density of the PRS as a function of time.

3.2. Magnetar Wind Nebula Model

K. Murase et al. (2016) and B. Margalit & B. D. Metzger (2018) have shown that a single expanding magnetized electron-ion nebula powered by a young magnetar can interact with the surrounding medium to produce synchrotron emission. The magnetar is assumed to inject energy into the nebula at a rate given by

$$\dot{E} = (\alpha - 1)\frac{E_{B_\star}}{t_0}\left(\frac{t}{t_0}\right)^{-\alpha} \quad \text{for } t \geqslant t_0, \ \ \alpha > 1, \tag{1}$$

where $E_{B_\star}$ is the free magnetic energy of the magnetar, α is a power-law index, and t_0 is the onset of the active period of the magnetar. The energy injection drives electrons through the surrounding medium, producing the observed persistent emission. At frequencies ν above the characteristic synchrotron self-absorption frequency $\nu_{\rm SSA}$, the synchrotron luminosity decays as follows (see B. Margalit & B. D. Metzger 2018, for detailed calculations):

$$L_\nu \propto \nu^{-\left(\frac{\alpha-1}{2}\right)} t^{-\frac{\alpha^2+7\alpha-2}{4}}. \tag{2}$$

We adopt Equation (2) and modify it as follows:

$$F(\nu, t) = A\, \nu^{-\left(\frac{\alpha-1}{2}\right)} \left(\frac{t_{\rm obs} + t_{\rm age}}{t_{\rm age}}\right)^{-\left(\frac{\alpha^2+7\alpha-2}{4}\right)}, \tag{3}$$

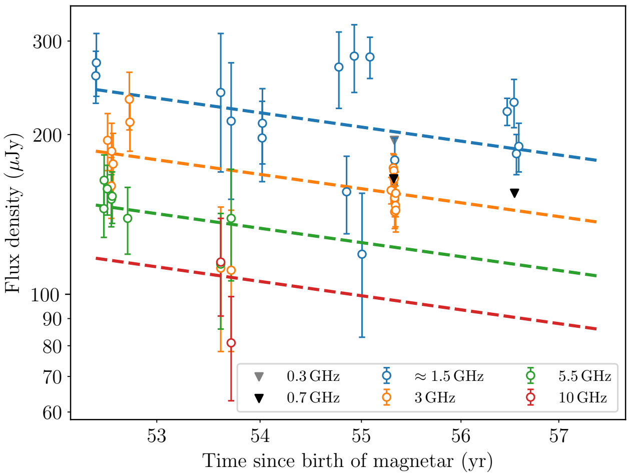

Figure 2. Light curve of the FRB 20190520B PRS, showing the joint spectrotemporal fit using Equation (3). This fit gives an estimate of the age of the persistent source to be $t_{\rm age} = 52$ yr.

Table 2
MCMC Posterior Best-fit Parameters for the Decay Using Equation (3)

Parameter	Prior Type	Bounds	Posterior Value
α	uniform	$(1, \infty)$	$1.77^{+0.07}_{-0.08}$
$t_{\rm age}$ (yr)	uniform	(4, 1900)	52^{+16}_{-10}
A (uJy)	uniform	$(1, \infty)$	284^{+18}_{-19}

where A is a scaling constant, $t_{\rm obs}$ is the time since the first observation of the PRS, $t_{\rm age}$ is the age of the persistent source at the time of the first observation. We perform a Markov Chain Monte Carlo (MCMC) fit of Equation (3) using the `emcee` package (D. Foreman-Mackey et al. 2013), incorporating all the detections listed in Table 1. The allowed range of the parameters is $\alpha > 1$ (from the assumption of the MWN model), 4 yr $< t_{\rm age} <$ 1900 yr (from S. Bhandari et al. 2023), and $A > 1$ μJy (a scaling parameter that is greater than 1 μJy can be deduced visually from Figure 1). The posterior distributions were analyzed using `ChainConsumer` (S. R. Hinton 2016), resulting in the best-fit parameters listed in Table 2. Figure 2 shows the best-fit light curves for different frequencies, following the color code of the data points. The corresponding best-fit spectra are shown in Figure 3. The best-fit age of the persistent source, $t_{\rm age}$, is 52^{+16}_{-10} yr, consistent with the allowed age limits derived in S. Bhandari et al. (2023), slightly higher than the 16–22 yr estimate from Z. Y. Zhao & F. Y. Wang (2021), and closer to the estimate of 40 yr from the magnetar-flare-powered model discussed in M. Bhattacharya et al. (2024). The best-fit energy injection power-law index is $\alpha = 1.77^{+0.07}_{-0.08}$. Excluding the flaring and dimming events observed in late 2022 does not significantly alter the best-fit parameter values.

In addition to the flux decay observed at frequencies $\nu > 1$ GHz, the upper limits from our uGMRT observations at $\nu < 1$ GHz (from the 2023 and 2024 epochs) suggest a spectral break between 700 MHz and 1.3 GHz (see blue shaded portion in Figure 3). At the observed timescales, such a spectral break is consistent with synchrotron self-absorption. However, the available upper limits are insufficient to constrain the synchrotron self-absorption frequency. Deeper observations

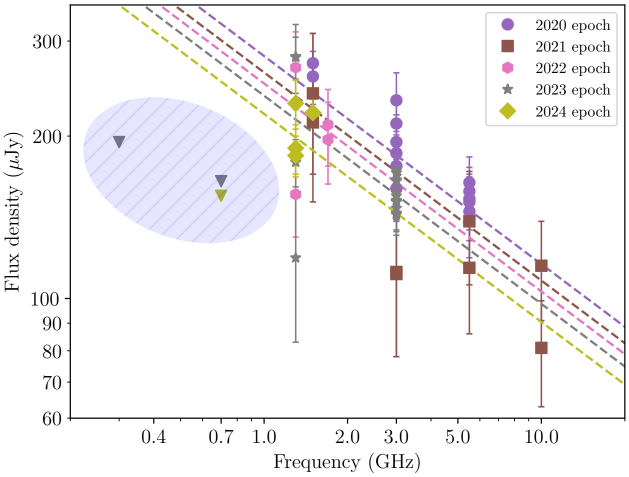

Figure 3. Spectrum of the PRS of FRB 20190520B showing the joint spectrotemporal fit using Equation (3). The color of the dashed lines represents the different epochs. The shaded blue region shows the uGMRT upper limits that suggest a break in the spectrum at frequencies <1 GHz.

at sub-GHz frequencies will be required to quantitatively determine the location of the spectral break. A recent study of the persistent emission from FRB 20240114A using GMRT, VLA, and MeerKAT data shows evidence of a synchrotron self-absorption peak at $\nu \approx 1.6$ GHz (X. Zhang et al. 2025), thereby agreeing with the spectral break below 1.3 GHz that we observe for the PRS associated with FRB 20190520B in this work.

3.3. *Scintillation as a Source of PRS Variability*

X. Zhang et al. (2023) analyzed temporal variability above 1 GHz and found no significant variation in most bands. A marginal variability was seen at 3 GHz. We extend the same variability analysis, adding our 1.3 GHz observations to the 1.5 GHz observations reported by X. Zhang et al. (2023). One of the causes of variability of a compact radio source is interstellar scintillation. Scintillation arises due to inhomogeneities in the ionized ISM and can cause apparent flux variations in compact radio sources. We follow the formalism introduced in R. Narayan (1992) and further explored in M. A. Walker (1998) for our analysis here. The scattering strength parameter ξ describes the scintillation due to a screen at a distance D from the observer. $\xi = 1$ corresponds to the critical value at which phase changes are substantial, across the characteristic first Fresnel zone $\theta_F = \sqrt{c/2\pi\nu D}$, where ν is the frequency of observation. Now, ξ is expressed as $(\nu_0/\nu)^{17/10}$, where ν_0 is the transition frequency between the weak scattering ($\xi \ll 1$ and $\nu_0 < \nu$), and strong scattering ($\xi \gg 1$ and $\nu_0 > \nu$) regimes. This transitional frequency has been estimated to be $\nu_0 = 12.53$ GHz using the galactic free electron density model in pyNE2001 (J. M. Cordes & T. J. W. Lazio 2002). Given $\nu_0 = 12.53$ GHz, we are in the strong scattering regime as $\nu_0 > \nu$ (as $\nu = 1.5$ GHz). There are two possible scintillation scenarios: diffractive scintillation and refractive scintillation. Diffractive scintillation is relevant at a characteristic frequency bandwidth, of $\xi^{-2}\nu = \nu(\nu_0/\nu)^{17/5}$, which is ~1 MHz for our observations. Our observations span a larger bandwidth, washing out diffractive scintillation. Hence, refractive scintillation is the relevant mechanism here. For refractive scintillation, the expected modulation index is

$$m_{\rm exp} = \xi^{-1/3} = \left(\frac{\nu}{\nu_0}\right)^{17/30} = 0.29. \tag{4}$$

Assuming a scattering disk at a distance of $D = 1$ kpc from us, the size of the Fresnel zone at $\nu = 1.4$ GHz is $\theta_F = \sqrt{c/2\pi\nu D} = 6.78\ \mu as$. Therefore, the angular size of the screen is

$$\theta_r = \theta_F \xi = 284.1\ \mu\text{as}. \tag{5}$$

This angular size of the screen can be converted to a projected radius of the screen at the distance of the source using the luminosity distance of the host galaxy (i.e., $d_{\rm lum} = 1218$ Mpc) as follows:

$$R_r = \theta_r d_{\rm lum}/2 = 5.0 \times 10^{18}\ \text{cm} = 1.68\ \text{pc}. \tag{6}$$

The characteristic timescale associated with the refractive scintillation from this screen is

$$t_r = 2\left(\frac{\nu_0}{\nu}\right)^{11/5} = 10.47\ \text{days}. \tag{7}$$

Given this expected timescale, we compute the modulation index of the observed data in the frequency range 1.3–1.7 GHz from Table 1, by averaging consecutive data that are within the refractive scintillation timescale, t_r, using the following expression:

$$m_{\rm obs} = \frac{1}{\overline{F_i}}\sqrt{\frac{N}{N-1}\left(\overline{F_i^2} - \overline{F_i}^2\right)}, \tag{8}$$

where F_i are the flux density measurements, $\overline{F_i}$ is the mean of the flux density measurements, $\overline{F_i^2}$ is the mean of the squares of F_i, and N is the total number of observations.

We obtain the observed modulation index $m_{\rm obs} = 0.23$. The observed modulation of the PRS flux is less than that expected from this region of the sky, i.e., $m_{\rm obs} < m_{\rm exp}$. This observation can be interpreted in the following ways:

1. All the variability observed is due to scintillation, and the pyNE2001 estimate of the transition frequency is accurate. However, the observed flux modulation is less than the expected modulation. This change in modulation can be explained if the size of the source θ_s is slightly larger than the size of the screen θ_r, reducing the modulation index by a factor of $(\theta_r/\theta_s)^{7/6}$, and increasing the refractive timescale by a factor of θ_s/θ_r (see M. A. Walker 1998, for details). Table 3 summarizes the possible constraints on the size of the source ($R_s = \theta_s d_{\rm lum}/2$), and the modified timescale of the scintillation, for screens at a distance of 0.1, 1, and 10 kpc. The projected screen radius (R_r) values listed in Table 3 can be quoted as a conservative lower limit of the size of the source. These are shown in Figure 4 for different distances of the screen from the observer in the $t_{\rm age}$–R_n phase space plot, adapted from S. Bhandari et al. (2023).
2. All the variability observed is due to scintillation, but the pyNE2001 model estimate of the transition frequency is not accurate. If this is the case, we can estimate the transition frequency required to produce the observed modulation. Table 3 lists the expected transition

Table 3

Scintillation Analysis and Predictions at $\approx$1.4 GHz (the Observation Frequency Used Is a Mean of All the Detections from Table 1, i.e., $\nu \approx 1.4$ GHz)

Dataset	t_r	$m_{\rm exp}$	$m_{\rm obs}$	Characteristic Sizes									Modified t_r	Modified ν_0
				$D = 0.1$ kpc			$D = 1$ kpc			$D = 10$ kpc				
	(days)			θ_F (μas)	R_r (pc)	R_s (pc)	θ_F (μas)	R_r (pc)	R_s (pc)	θ_F (μas)	R_r (pc)	R_s (pc)	(days)	(GHz)
Data as it is	10.47	0.29	0.23	21.44	5.30	6.48	6.78	1.68	2.05	2.14	0.53	0.65	12.80	18.93
Removed best-fit decay	...	...	0.22	...	...	6.80	...	...	2.15	...	...	0.68	13.43	20.92

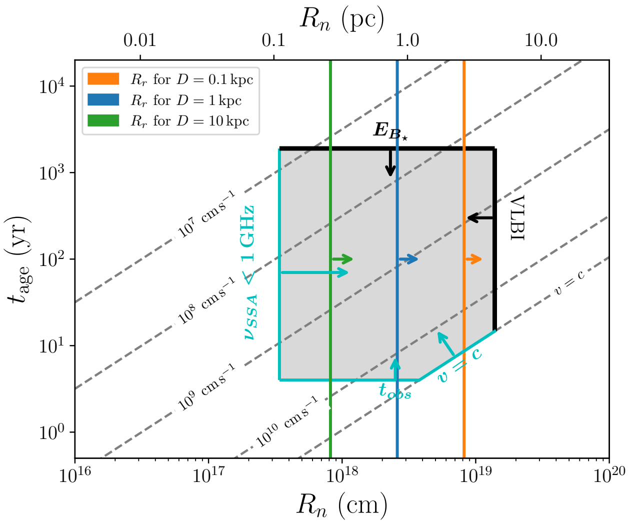

Figure 4. Constraint on the radius of the PRS source using the projected size of the screen R_r. The figure is adapted from S. Bhandari et al. (2023), after correcting for the radius by dividing all limits by 2.

   frequency, ν_0, which can produce the observed modulation index at $\nu = 1.4$ GHz.
3. All the variability observed is intrinsic to the source. This implies that the size of the source θ_s is larger than the size of the screen θ_r, and therefore, refractive scintillation (which assumes a point source) is not relevant here. The projected size of the screen R_r tabulated in Table 3 can be used as a conservative lower limit of the size of the source in this case.

At this point, we also note that there is a possibility of both intrinsic variability and scintillation contributing to the observed variability. It is not trivial to separate the two without independent constraints on the size of the source and the properties of the scattering screen.

For completeness, we also repeat this analysis after removing the expected decay from the MWN model (Section 3.2). The inferred size and timescale constraints remain broadly consistent in both cases.

3.4. Hypernebula Model

Another model proposed to explain the PRSs associated with FRBs is the hypernebula model (N. Sridhar & B. D. Metzger 2022). In this model, mass transfer from a companion star onto a massive black hole via Roche-lobe overflow drives powerful disk winds. These winds inflate a bubble of relativistic electrons that emit synchrotron radiation. Two key timescales characterize the model: the timescale over which the wind expands freely into the circumstellar medium, $t_{\rm free}$; and $t_{\rm active} \sim 10$–10^6 yr, the total duration of the accretion phase (N. Sridhar & B. D. Metzger 2022). The relatively modest evolution in burst DM over time (C. H. Niu et al. 2022; R. Anna-Thomas et al. 2023) suggests that the system is currently at $t < t_{\rm free}$. However, Z. Y. Zhao & F. Y. Wang (2021) show a decreasing trend in the burst DM. N. Sridhar & B. D. Metzger (2022) applied the hypernebula model specifically to FRB 20190520B, using a set of best-fit model parameters (e.g., age, mass accretion rate, and ambient density) chosen to match the source's known properties at the time. For those specific parameters, their model predicts a gradual increase in radio flux of the PRS at GHz frequencies over decadal timescales—this is explicitly stated in Section 4.2 of their paper and shown in their model curves (see Figures 5 and 6 in N. Sridhar & B. D. Metzger 2022). Whereas, we see a slow decay in the flux over the span of ∼4 yr. This is in contrast to our observations, indicating that the best-fit hypernebula model using data from the first 2 yr since detection is inconsistent with the recent observed behavior of the PRS associated with FRB 20190520B.

3.5. Active Galactic Nucleus or Intermediate Mass Black Hole Origin for the Persistent Radio Source

An alternative scenario is that the PRS associated with FRB 20190520B is physically unrelated to the FRB engine, and instead arises from accretion onto a massive black hole, as discussed by R. Anna-Thomas et al. (2023). In this picture, the PRS represents compact synchrotron emission from a radio-loud, low-Eddington active galactic nucleus (AGN), while the FRB originates from a separate compact object—such as a magnetar—embedded within the same nuclear environment.

Recent work by Y. Dong et al. (2024) has systematically compared the radio spectra of persistent sources in nearby dwarf galaxies—including known low-mass AGNs—with those of FRB-associated PRSs, including FRB 20190520B and FRB 20121102A. They find that several AGNs in dwarf hosts exhibit flat or slightly inverted radio spectra and luminosities consistent with both FRB PRSs, suggesting that an AGN origin cannot be ruled out based on spectral properties alone.

For FRB 20190520B, the persistent source exhibits a flat spectrum, compact morphology (unresolved on ∼10 pc scales), and high radio luminosity ($L_\nu \sim 3 \times 10^{29}$ erg s^{-1} Hz^{-1}), all of which are consistent with a jet-dominated AGN powered by an intermediate mass black hole (IMBH). Importantly, recent XMM-Newton and Chandra observations place an upper limit on the X-ray luminosity of $L_X \lesssim 9 \times 10^{42}$ erg s^{-1} (3σ) (Z. Yan et al. 2025), which yields a radio-to-X-ray luminosity ratio of $\log(R_X) \gtrsim -3$. This value lies within the regime of radio-loud AGNs (Y. Terashima & A. S. Wilson 2003), and is broadly consistent with radiatively inefficient accretion flows.

A similar interpretation has been proposed for the PRS associated with FRB 20121102A. M. Bhardwaj et al. (2025) argued that its long-term flux stability, compact size (<0.35 pc), and placement on the radio-loud fundamental plane of black hole activity can be explained by a low-Eddington AGN powered by an IMBH. Given the morphological and spectral similarities between the two sources, a comparable AGN origin for the PRS of FRB 20190520B remains observationally viable. However, as with FRB 20121102A, this model requires that the FRB bursts themselves arise from a distinct, colocated source within the broader accretion environment.

Further high-resolution radio monitoring and deep X-ray observations will be essential to distinguish between AGN and MWN interpretations and to assess whether FRB sources and persistent emitters are causally connected or merely cohabit similar extreme environments.

4. Conclusion

In this paper, we present broadband radio observations (0.3–10 GHz) of the PRS associated with FRB 20190520B. We analyze the data under different proposed models and comment on the physics responsible for the observed emission. The findings are summarized below.

1. We observe a slow decay in the brightness of the PRS with time across all frequency bands. There are episodes of brightening and dimming seen in the 1.5 and 3 GHz data.
2. The first low-frequency (<1 GHz) observations of this PRS hint at a spectral break between ≈0.7 GHz and ≈1.3 GHz, which can be attributed to synchrotron self-absorption. It is not possible to estimate the self-absorption frequency using only the upper limits from the low-frequency observations presented here.
3. We fit the decaying light curves at all frequencies using the decay equation described in Equation (3), derived from the MWN model. This resulted in an estimate of the power-law index for energy injection $\alpha = 1.77^{+0.07}_{-0.08}$ and the age of the magnetar is $t_{\rm age}$, is 52^{+16}_{-10} yr. These values are in agreement with constraints from previous observations of the PRS (Z. Y. Zhao & F. Y. Wang 2021; S. Bhandari et al. 2023; M. Bhattacharya et al. 2024).
4. We also comment on the contribution of scintillation to the variability of the PRS at 1.5 GHz. Through this analysis, a conservative lower limit on the size of the source >0.53 pc (for a screen at 10 kpc) is derived (assuming that NE2001 accurately models the transition frequency and that the observed variability is due to scintillation). This limit is consistent with constraints from VLBI observations and low-frequency nondetection. We also note that the variability could be a combination of scintillation and intrinsic variability, and it is not trivial to distinguish between the two.
5. Finally, we discuss the observations under the purview of the best-fit hypernebula model for the PRS associated with FRB 20190520B presented in N. Sridhar & B. D. Metzger (2022). This best-fit model predicts a rise in flux with time at 1.5 GHz, which does not agree with the observations presented here.

Ongoing monitoring of known PRSs, along with future detections of new PRSs associated with FRBs, will be crucial in further constraining the emission mechanisms and understanding the role of the local environment in the persistent emission.

Acknowledgments

We thank the staff of the GMRT who made these observations possible. GMRT is run by the National Centre for Radio Astrophysics of the Tata Institute of Fundamental Research. The National Radio Astronomy Observatory is a facility of the National Science Foundation operated under cooperative agreement by Associated Universities, Inc. M.B. is a McWilliams fellow and an International Astronomical Union Gruber fellow. M.B. also receives support from the McWilliams seed grant. Finally, we gratefully acknowledge the insightful discussions held during the FRB Frontiers Meeting (2025 March 3–5), which contributed significantly to the development of this work (M. Bhardwaj & M. McLaughlin 2025). A.B. thanks Deepak Eappachen for useful discussions.

Software: CASA (CASA Team et al. 2022), CASA CAPTURE (R. Kale & C. H. Ishwara-Chandra 2021), emcee (D. Foreman-Mackey et al. 2013), ChainConsumer (S. R. Hinton 2016), Astropy (Astropy Collaboration et al. 2013, 2018, 2022), NumPy (C. R. Harris et al. 2020), SciPy (P. Virtanen et al. 2020), Matplotlib (J. D. Hunter 2007).

Appendix
Comparison of Calibration of Images

This section contains a comparison of the image of the target PRS along with the calibrator, 3C286 to demonstrate the calibrations errors present in the 2022 November 11 data. This is shown in Figure A1.

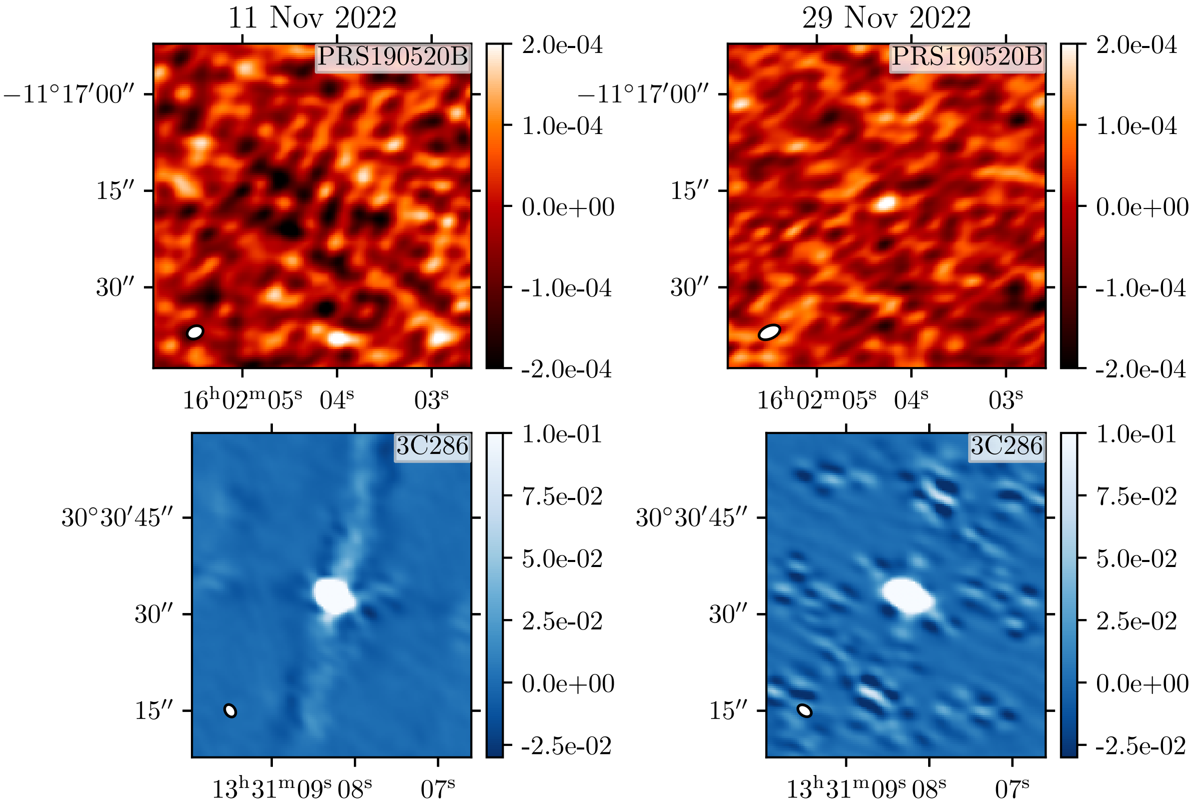

Figure A1. Comparison of the image of the target PRS (top row) and the calibrator 3C286 (bottom row) on 2022 November 11 (left column) and 2022 November 29 (right column). This shows the calibration errors in the 2022 November 11 data.

ORCID iDs

Arvind Balasubramanian https://orcid.org/0000-0003-0477-7645
Mohit Bhardwaj https://orcid.org/0000-0002-3615-3514
Shriharsh P. Tendulkar https://orcid.org/0000-0003-2548-2926

References

Anna-Thomas, R., Connor, L., Dai, S., et al. 2023, Sci, 380, 599
Astropy Collaboration, Price-Whelan, A. M., Lim, P. L., et al. 2022, ApJ, 935, 167
Astropy Collaboration, Price-Whelan, A. M., Sipőcz, B. M., et al. 2018, AJ, 156, 123
Astropy Collaboration, Robitaille, T. P., Tollerud, E. J., et al. 2013, A&A, 558, A33
Bhandari, S., Marcote, B., Sridhar, N., et al. 2023, ApJL, 958, L19
Bhardwaj, M., Balasubramanian, A., Kaushal, Y., & Tendulkar, S. P. 2025, PASP, 137, 084202
Bhardwaj, M., & McLaughlin, M. 2025, NatAs, 9, 945
Bhardwaj, M., Snelders, M. P., Hessels, J. W. T., et al. 2025, ApJL, 992, L35
Bhattacharya, M., Murase, K., & Kashiyama, K. 2024, arXiv:2412.19358
Bhusare, Y., Maan, Y., & Kumar, A. 2025, ApJ, 993, 234
Bochenek, C. D., Ravi, V., Belov, K. V., et al. 2020, Natur, 587, 59
Bruni, G., Piro, L., Yang, Y.-P., et al. 2024, Natur, 632, 1014
CASA Team, Bean, B., Bhatnagar, S., et al. 2022, PASP, 134, 114501
Chatterjee, S., Law, C. J., Wharton, R. S., et al. 2017, Natur, 541, 58
Chen, X.-L., Tsai, C.-W., Stern, D., et al. 2025, ApJ, 982, 203
CHIME/FRB Collaboration, Amiri, M., Andersen, B. C., et al. 2021, ApJS, 257, 59
CHIME/FRB Collaboration, Amiri, M., Andersen, B. C., et al. 2024, ApJ, 969, 145
CHIME/FRB Collaboration, Andersen, B. C., Bandura, K. M., et al. 2020, Natur, 587, 54
Cordes, J. M., & Lazio, T. J. W. 2002, arXiv:astro-ph/0207156
Dong, Y., Eftekhari, T., Fong, W., et al. 2024, ApJ, 973, 133
Foreman-Mackey, D., Hogg, D. W., Lang, D., & Goodman, J. 2013, PASP, 125, 306
Harris, C. R., Millman, K. J., van der Walt, S. J., et al. 2020, Natur, 585, 357
Hinton, S. R. 2016, JOSS, 1, 00045
Hunter, J. D. 2007, CSE, 9, 90
Hussain, M., & Mahmud, I. 2019, JOSS, 4, 1556
Ibik, A. L., Drout, M. R., Gaensler, B. M., et al. 2024, ApJ, 976, 199
Kale, R., & Ishwara-Chandra, C. H. 2021, ExA, 51, 95
Lee, K.-G., Khrykin, I. S., Simha, S., et al. 2023, ApJL, 954, L7
Li, D., Wang, P., Qian, L., et al. 2018, IMMag, 19, 112
Lorimer, D. R., Bailes, M., McLaughlin, M. A., Narkevic, D. J., & Crawford, F. 2007, Sci, 318, 777
Marcote, B., Nimmo, K., Hessels, J. W. T., et al. 2020, Natur, 577, 190
Margalit, B., & Metzger, B. D. 2018, ApJL, 868, L4
Moroianu, A. M., Bhandari, S., Drout, M. R., et al. 2025, arXiv:2509.05174
Murase, K., Kashiyama, K., & Mészáros, P. 2016, MNRAS, 461, 1498
Narayan, R. 1992, RSPTA, 341, 151
Niu, C. H., Aggarwal, K., Li, D., et al. 2022, Natur, 606, 873
Petroff, E., Hessels, J. W. T., & Lorimer, D. R. 2022, A&ARv, 30, 2
Platts, E., Weltman, A., Walters, A., et al. 2019, PhR, 821, 1
Sridhar, N., & Metzger, B. D. 2022, ApJ, 937, 5
Tendulkar, S. P., Gil de Paz, A., Kirichenko, A. Y., et al. 2021, ApJL, 908, L12
Terashima, Y., & Wilson, A. S. 2003, ApJ, 583, 145
Virtanen, P., Gommers, R., Oliphant, T. E., et al. 2020, NatMe, 17, 261
Walker, M. A. 1998, MNRAS, 294, 307
Xu, J., Feng, Y., Li, D., et al. 2023, Univ, 9, 330
Xu, J., Tsai, C.-W., Lake, S. E., et al. 2025, Univ, 11, 206
Yan, Z., Yu, W., Page, K. L., et al. 2025, ApJ, 983, 116
Yang, A. Y., Feng, Y., Tsai, C.-W., et al. 2024, ApJ, 976, 165
Zhang, X., Yu, W., Law, C., et al. 2023, ApJ, 959, 89
Zhang, X., Yu, W., Yan, Z., Xing, Y., & Zhang, B. 2025, arXiv:2501.14247
Zhao, Z. Y., & Wang, F. Y. 2021, ApJL, 923, L17